

# Magnified or multiply imaged? – Search strategies for gravitationally lensed supernovae in wide-field surveys

Radosław Wojtak<sup>1\*</sup>, Jens Hjorth<sup>1</sup> and Christa Gall<sup>1</sup>

<sup>1</sup>*DARK, Niels Bohr Institute, University of Copenhagen, Lyngbyvej 2, 2100 Copenhagen, Denmark*

4 June 2019

## ABSTRACT

Strongly lensed supernovae can be detected as multiply imaged or highly magnified transients. In order to compare the performances of these two observational strategies, we calculate expected discovery rates as a function of survey depth in five *grizy* filters and for different classes of supernovae (types Ia, IIP, IIL, Ibc and IIn). We find that detections via magnification is the only effective strategy for relatively shallow pre-LSST surveys. For survey depths about the LSST capacity, both strategies yield comparable numbers of lensed supernovae. Supernova samples from the two methods are to a large extent independent and combining them increases detection rates by about 50 per cent. While the number of lensed supernovae detectable via magnification saturates at the limiting magnitudes of LSST, detection rates of multiply imaged supernova still go up drastically at increasing survey depth. Comparing potential discovery spaces, we find that lensed supernovae found via image multiplicity exhibit longer time delays and larger image separations making them more suitable for cosmological constraints than their counterparts found via magnification.

We provide useful fitting functions approximating the computed discovery rates for different supernova classes and detection methods. We find that the Zwicky Transient Factory will find about 2 type Ia and 4 core-collapse lensed supernovae per year at a limiting magnitude of 20.6 in the *r* band. Applying a hybrid method which combines searching for highly magnified or multiply imaged transients, we find that LSST will detect 89 type Ia and 254 core-collapse lensed supernovae per year. In all cases, lensed core-collapsed supernovae will be dominated by type IIn supernovae contributing to 80 per cent of the total counts, although this prediction relies quite strongly on the adopted spectral templates for this class of supernovae. Revisiting the case of the lensed supernova iPTF16geu, we find that it is consistent within the  $2\sigma$  contours of predicted redshifts and magnifications for the iPTF survey.

**Key words:** supernovae: general – gravitational lensing: strong – methods: statistical

## 1 INTRODUCTION

The phenomenon of strongly lensed (multiply imaged) supernovae has long been theoretically considered (Refsdal 1964), but the first detections became possible only very recently. Quimby et al. (2014) found a strongly lensed Type Ia supernova magnified by a factor of 30, although multiple images were not resolved. The first fully resolved image configuration of a lensed supernova was reported by Kelly et al. (2015). The supernova (SN Refsdal) was a core-collapse type (Kelly et al. 2016) and lensed by an intervening galaxy cluster and a massive galaxy in the cluster. The second example of a fully resolved lensed supernova was iPTF16geu

(Goobar et al. 2017). Detected as an exceptionally luminous supernova (for its redshift) in a regular transient survey, the intermediate Palomar Transient Factory (iPTF), it was subsequently observed by ESO VLT, Keck Observatory, and the Hubble Space Telescope whose images revealed a quadrupole lensing configuration with a sub-arcsec scale of image separations. The supernova was classified as a type Ia SN (Goobar et al. 2017; Cano et al. 2018). High-cadence imaging of massive galaxy clusters with HST also recently resulted in the discovery of a new type of lensed transients which appeared to be strongly lensed individual stars (Rodney et al. 2018; Kelly et al. 2018; Chen et al. 2019; Kurov et al. 2019).

Strongly lensed supernovae are unique objects in several respects, making them a promising tool for constraining cosmological parameters such as the Hubble constant

\* E-mail: radek.wojtak@nbi.ku.dk

(Grillo et al. 2018; Vega-Ferrero et al. 2018). With well-studied light curves, reasonably well-represented by simple models, lensed supernovae appear to be suitable for precise measurements of time delays from even relatively short observing campaigns (Rodney et al. 2016). If, in addition, a lensed supernova is of Type Ia, extra constraints from the standard candle nature come into play. This can be used to measure magnification in an independent way (Rodney et al. 2015) and thus provide additional constraints on the lens model. This extra information can potentially narrow down inherent degeneracies in lens models which leave all lensing observables invariant, except the time delay (Schneider & Sluse 2014). The unresolved degeneracies are the main source of potential systematic errors in cosmological constraints obtained from time-delay observations (Kolatt & Bartelmann 1998; Oguri & Kawano 2003).

Strongly lensed supernovae will be found in large numbers and in a more automatic way in ongoing and future transient surveys (see e.g. Diego 2018). Two possible strategies for finding plausible candidates can be considered. One can search for multiply imaged supernovae (Oguri & Marshall 2010) or highly magnified (unresolved) transients (Goldstein & Nugent 2017). The former probes a unique feature indicating unambiguously the lensing nature of a candidate. The latter approach is less direct and involves an estimate of how much brighter an observed supernova is compared to a fiducial reference supernova, as it would have been observed in the lens galaxy (or the apparent host galaxy). Atypically bright supernovae in this case would indicate a high chance of observing a higher-redshift, gravitationally magnified (amplified) supernova.

Searching for lensed supernovae via image multiplicity or magnification are the main observational strategies based on two characteristic features of the lensing phenomenon. The expected discovery rates have been estimated in several studies; however, each of them considering only one of the two methods and adopting specifications of upcoming surveys (Oguri & Marshall 2010; Goldstein & Nugent 2017; Goldstein et al. 2018a). At present, it is unclear to what extent the two methods are equivalent or complementary, which technique is more effective in finding lensed supernovae in different ranges of limiting magnitudes or whether one would benefit from combining them. The two methods may differ not only in terms of their performance in finding candidates, but also in terms of the characteristics of the resulting lensed supernova samples. This in turn raises the question which supernova sample and thus which method would be suitable for robust measurements of time delays for the purpose of cosmological inference. In order to address these issues, we compute detection rates for both methods and a wide range of possible filters and supernova types. This allows us to make the first comprehensive comparison of detection methods in terms of the discovery potential and the cosmological constraining power of the expected gravitationally lensed supernova samples. We explore the possibilities of boosting discovery rates by combining the methods and we revisit the estimates of detection rates for ongoing and upcoming transient surveys.

Estimating discovery rates of gravitationally lensed supernovae is not merely a means for quantifying the efficiency of detection methods. Lensed supernovae can be also regarded as a cosmological tool probing a wide range of phys-

ical properties across cosmic time, e.g. volumetric rates and luminosity functions of supernovae, lens models or cosmological parameters. Observed detection rates can potentially shed light on some aspects of our current models.

The paper is organized as follows. Section 2 outlines detection methods and the potential of increasing their discovery potential by combining them. We describe the computation of discovery rates as well as the underlying lens model and volumetric supernova rates in Section 3. The results are presented in Section 4 followed by a discussion in Section 5 and concluding remarks in Section 6. We adopt a flat  $\Lambda$ CDM cosmological model with  $\Omega_m = 0.3$  and  $H_0 = 73 \text{ km s}^{-1} \text{ Mpc}^{-1}$ .

## 2 OBSERVATIONAL STRATEGIES

The two main features through which strong lensing manifests itself are the multiplicity of images and the magnification of each image. Therefore, strongly lensed supernovae can be detected and distinguished from ordinary non-lensed supernovae if they appear as spatially and temporarily coincident transients (Oguri & Marshall 2010) or exceptionally bright transients (Goldstein & Nugent 2017). In the following, we outline each observational strategy and the related detection criteria in more detail.

### 2.1 Image multiplicity

The critical factors for detecting multiple images are the image separations relative to the seeing, the flux contrast between the images and the apparent magnitudes of the faintest images in the configuration. As a base model for this strategy we adopt detection criteria optimized for the Large Synoptic Sky Survey (LSST), as proposed by Oguri & Marshall (2010). Following this approach, a transient is identified as a strongly lensed supernova if *i.* the maximum image separation  $\theta_{\text{max}}$  between images falls into a range between  $0.5''$  and  $4''$ , where these limits stem from seeing conditions as well as the choice of selecting systems lensed by isolated galaxies, characterized by relatively simple lens models, *ii.* the flux ratio between the images for doubly imaged supernovae is larger than 0.1 and *iii.* at least three or two images are detected for quads/cusps (four/three images) and doubles (two images), respectively. For sufficiently bright supernovae and a suitable survey cadence, this strategy not only yields detections of multiply imaged supernovae, but it also enables the measurement of basic lensing properties such as time delays and flux ratios between the images. In this respect, this is an ideal observational strategy for large and self-contained surveys such as the LSST. Initial information on lensing configurations can be also used to pin down the best candidates for follow-up observations.

### 2.2 Magnification

Strongly lensed supernovae can be detected as transients which appear significantly brighter than the brightest supernovae at the redshift of the apparent host galaxy (lens galaxy for lensed supernovae or actual host galaxy for non-lensed transients). Following Goldstein & Nugent (2017), the

detection criterion can be formulated in the following way:

$$m_X(t_{\text{peak}}) < \langle M_X \rangle(t_{\text{peak}}) + \mu(z_{\text{host}}) + K_{XX}(z_{\text{host}}, t_{\text{peak}}) + \Delta m, \quad (1)$$

where  $m_X(t_{\text{peak}})$  is the observed peak magnitude of the transient in band  $X$ ,  $\langle M_X \rangle(t_{\text{peak}})$  is a mean absolute magnitude of a reference class of brightest supernovae in band  $X$  at peak,  $\mu$  is the distance modulus,  $z_{\text{host}}$  is redshift of the apparent host galaxy,  $K_{XX}(z_{\text{host}}, t_{\text{peak}})$  is a K-correction for the assumed reference class of brightest supernovae at the peak of their light curves and  $\Delta m < 0$  is a free parameter defining the magnitude gap between lensed and non-lensed supernovae. Absolute magnitudes and K-corrections can be calculated from spectral templates of the assumed reference class of bright supernovae, while the redshift of the apparent host galaxy can be estimated from existing photometric data from wide-field surveys. Since only rare cases of supernovae are brighter than SNe Ia, e.g. superluminous supernovae, it is reasonable to use type Ia as the reference class of bright supernovae. Like Goldstein & Nugent (2017), we assume a mean peak absolute magnitude of  $-19.3$  in the  $B$  band.

The choice of the parameter  $\Delta m$  is dictated by a trade-off between the completeness and the contamination of the selected lensed supernova candidates. As a base model, we use  $\Delta m = -0.7$  required for distinguishing between the brightest non-lensed type Ia supernovae and gravitationally lensed supernovae (Goldstein & Nugent 2017). We expect that the assumed magnitude gap is a sufficiently conservative choice from the point of view of minimizing the false positive rate. However, one has to bear in mind that rare luminous supernovae brighter than  $-20$  in the  $B$  band inevitably will be confused with lensed supernovae in this approach.

The effective depth of a transient survey in the context of detecting strongly lensed supernovae via magnification is modulated by the extent to which all lensing images contribute to the measured flux. It is natural to consider here two scenarios in which the total observed flux either comes from all images or is simply approximated by the flux of the brightest image. The former, which we adopt as our base model, sets an upper limit on the effective depth and discovery rates with respect to how efficiently the measured flux is integrated over all images. The latter determines the corresponding lower limits. We expect that most realistic detections in typical transient surveys will be intermediate between the two extremes.

Compared to the strategy based on detection of multiple images, the competitiveness of this method heavily relies on follow-up observations. Higher resolution and deeper observations are necessary to both confirm the lensing nature of the candidates (by means of detecting multiple images) and determining the lensing configuration.

Although initially envisaged for finding strongly lensed type Ia supernovae, the method can be also applied to detecting gravitationally lensed core-collapse supernovae (Goldstein et al. 2018a). Here, using type Ia supernovae as the reference class of bright supernovae sets a relatively conservative detection threshold. However, as we shall see, the higher volumetric rates of core-collapse supernovae can compensate their lower luminosities leading to even higher discovery rates than for type Ia.

### 2.3 Hybrid approach

As we shall see in Section 4, the two methods described perform very differently. The methods are complementary in many respects in that they maximize their efficiencies in different ranges of survey depth. This provides motivation for considering a third approach which combines the ideas underlying the two techniques. Here, a transient is classified as a lensed supernova candidate if at least one of the two methods identifies it as a potential lensed supernova.

## 3 SIMULATIONS

We employ a Monte Carlo approach to compute the expected number of observed strongly lensed supernovae. The method relies on drawing random realizations of lens galaxies and supernovae in a light cone, and counting strong lensing events which satisfy certain detection conditions.

### 3.1 Lens galaxies

Motivated by its success in modeling multiply imaged QSOs, we assume that the mass distribution in the lens galaxies is adequately represented by a Singular Isothermal Ellipsoid (SIE) model (Kormann et al. 1994) in which the convergence  $\kappa$  is given by:

$$\kappa(x, y) = \frac{\theta_E}{2} \frac{\lambda(e)}{\sqrt{(1-e)^{-1}x^2 + (1-e)y^2}}, \quad (2)$$

$$\theta_E = 4\pi \left(\frac{\sigma}{c}\right)^2 \frac{D_{\text{ls}}}{D_s}, \quad (3)$$

where  $\theta_E$  is the Einstein radius,  $\sigma$  is the line-of-sight velocity dispersion of the lens galaxy,  $D_s$  and  $D_{\text{ls}}$  are angular diameter distances, respectively, between the observer and the source, and the lens galaxy and the source. The convergence depends on the shape of the lens galaxy through the ellipticity  $e$  of the projected lensing mass surface density, which includes the contributions from dark matter and baryonic components, both relevant for the statistics of strong lensing images (Castro et al. 2018). We assume that the ellipticity is given by the light distribution. Based on observational constraints, we adopt a Gaussian distribution for the ellipticity with a mean of 0.3 and dispersion of 0.16, with a truncation at 0.1 and 0.9 (Oguri et al. 2008). The function  $\lambda(e)$  is the so-called dynamical normalization and it depends on the deprojected shape of the lens galaxy. Following Chae (2003), we assume that both oblate and prolate ellipsoids approximate the actual shapes of lens galaxies with equal probabilities, implying  $\lambda(e) \approx 1$ .

In order to make the simulated lensing more realistic, we account for the effect of the lens environment by including external shear (Kochanek 1991; Witt & Mao 1997; Keeton et al. 1997) with a potential given by

$$V(x, y) = \frac{\gamma}{2}(x^2 - y^2) \cos(2\theta_\gamma) + \gamma xy \sin(2\theta_\gamma), \quad (4)$$

where  $\gamma$  is the magnitude of the external shear and  $\theta_\gamma$  is its position angle on the image plane. We assume that  $\gamma$  follows a log-normal distribution with mean 0.05 and dispersion 0.2 dex, as expected for the external shear around early-type galaxies, calculated by ray tracing in cosmological

simulations of the standard cosmological model (Holder & Schechter 2003). We expect that the employed simulation-based calibration of the external shear to a large extent accounts for lensing effects from realistic structures around lens elliptical galaxies, although the presence of a galaxy cluster may in addition affect the image configuration. The external shear in our model is uncorrelated with the orientation of the lens galaxy, i.e. it has a random orientation in the image plane.

We model the mass function of lens galaxies in terms of the velocity dispersion function of early-type galaxies, which are most common lens galaxies. The velocity dispersion function is well approximated by a modified Schechter function of the following form:

$$\frac{dn}{d\sigma} = \phi_* \left( \frac{\sigma}{\sigma_*} \right)^\alpha \exp \left[ - \left( \frac{\sigma}{\sigma_*} \right)^\beta \right] \frac{\beta}{\Gamma(\alpha/\beta)} \frac{1}{\sigma}, \quad (5)$$

where  $n$  is the comoving density of galaxies. We use the above probability density to draw random realizations of lens galaxies in our calculations. We adopt parameters derived from fitting this model to the SDSS data (Choi et al. 2007), i.e.

$$\begin{aligned} \phi_* &= 8.0 \times 10^{-3} h^3 \text{Mpc}^{-3} \\ \sigma_* &= 161 \text{ km s}^{-1} \\ \alpha &= 2.32 \\ \beta &= 2.67. \end{aligned} \quad (6)$$

Following Goldstein & Nugent (2017), we narrow the range of velocity dispersions to ( $50 \text{ km s}^{-1}, 400 \text{ km s}^{-1}$ ) for galaxies which can effectively act as gravitational lenses. The lower limit coincides also with the minimum velocity dispersion measured from the SDSS spectroscopic observations.

We assume that the velocity dispersion function does not evolve with redshift. Although observational constraints on the velocity dispersion function are limited at high redshifts, this assumption is corroborated by existing data showing no evidence of redshift evolution at  $z \lesssim 1$ , especially for the high velocity dispersion tail (Montero-Dorta et al. 2017; Bezanson et al. 2011). The assumption is also supported by theoretical arguments based on the standard model for halo formation, for which Mitchell et al. (2005) showed that the normalization of the velocity dispersion function can be higher only by  $\sim 15$  per cent at redshift  $z = 1$ , at which only rare galaxies can generate strongly lensed images of high-redshift supernovae detectable in surveys with depths comparable to the LSST.

The number of lens galaxies in an observational cone as a function of redshift and velocity dispersion is given by

$$\frac{dN_{\text{lens}}}{d\sigma dz} = 4\pi \frac{c}{H_0} \frac{(1+z)^2 D_A^2}{E(z)} \phi(\sigma), \quad (7)$$

where  $D_A$  is the angular diameter distance, and  $E(z) = H(z)/H_0$  is the dimensionless Hubble parameter. We note that the simulated redshift distribution of lens galaxies is independent of the Hubble constant adopted in our work and the only role of the assumed cosmological model is to extrapolate the redshift distribution from the redshifts of the main galaxy sample in the SDSS to higher redshifts.

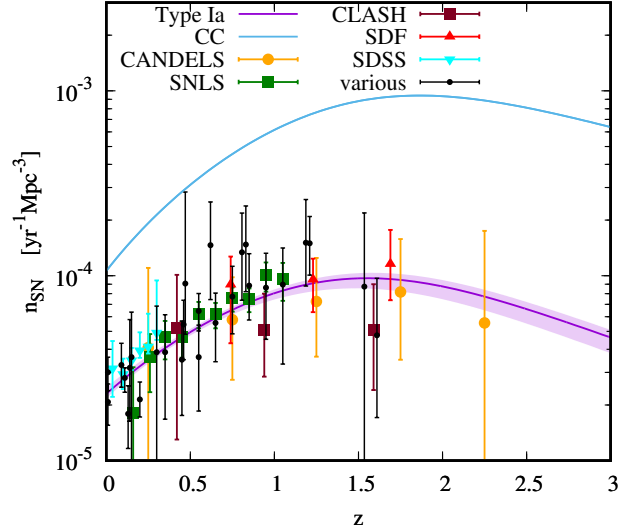


**Figure 1.** Comoving volumetric rate of type Ia and core-collapse supernovae assumed in our study. For core-collapse type, the rate is given by the star formation history from Madau & Dickinson (2014); for type Ia, the rate is the convolution of a delay time distribution given by eq. (11) with the adopted model of star formation history. Data points show observational measurements of the rate for type Ia, as compiled by Graur et al. (2014). The various distinct symbols highlight selected results from CANDELS (Rodney et al. 2014), the Supernova Legacy Survey (SNLS Perrett et al. 2012), the Cluster Lensing And Supernova survey with Hubble (CLASH Graur et al. 2014), the Subaru Deep Field (SDF Graur et al. 2011) and the Sloan Digital Sky Survey (SDSS Dilday et al. 2010). Black symbols include results from Graur & Maoz (2013); Barbary et al. (2012); Melinder et al. (2012); Li et al. (2011); Rodney & Tonry (2010); Botticella et al. (2008); Dahlen et al. (2008); Dilday et al. (2008); Horesh et al. (2008); Blanc et al. (2004); Tonry et al. (2003); Pain et al. (2002); Hardin et al. (2000); Cappellaro et al. (1999).

### 3.2 Supernovae

The total number of observed supernovae per unit time as a function of redshift is given by

$$\frac{dN_{\text{SN}}}{dz} = 4\pi \frac{c}{H_0} \frac{(1+z)^2 D_A^2}{E(z)} \frac{1}{1+z} n_{\text{SN}}(z), \quad (8)$$

where  $n_{\text{SN}}(z)$  is the volumetric supernova rate in a local rest frame. Compared to eq. (7), the additional factor  $1/(1+z)$  accounts for a conversion from a local to the observer rest frame.

We compute the volumetric type Ia supernova rate as the convolution of the delay time distribution  $\text{DTD}(t)$  with the star formation history  $\psi(t)$ , i.e.

$$n_{\text{SNIa}}(t) = \int_0^t \psi(t-\tau) \text{DTD}(\tau) d\tau. \quad (9)$$

For the star formation history, we employ a model from Madau & Dickinson (2014), based on a compilation of the cosmic star formation rates determined from UV and IR observations:

$$\psi(z) = 0.015 \frac{(1+z)^{2.7}}{1 + [(1+z)/2.9]^{5.6}} M_\odot \text{ yr}^{-1} h_{70} \text{ Mpc}^{-3}. \quad (10)$$

Following Rodney et al. (2014), we assume that the delay

time distribution is accurately described by the following piecewise function:

$$\text{DTD}(t) = \begin{cases} 0 & \text{if } t < 0.04 \text{ Gyr} \\ \eta_1 & \text{if } 0.04 \text{ Gyr} < t < 0.5 \text{ Gyr} \\ \eta_0 t^{-1} & \text{if } t > 0.5 \text{ Gyr} \end{cases} \quad (11)$$

where  $\eta_0$  and  $\eta_1$  are free parameters. This model is well motivated by observations (Rodney et al. 2014; Andersen & Hjorth 2018) as well as theoretical arguments derived from the evolution of binary systems (Maoz & Mannucci 2012). It accounts both for the population of prompt supernovae with delay time  $t < 0.5$  Gyr (with 40 Myr as the shortest possible time before explosion, Belczynski et al. 2005) and delayed supernovae with  $\text{DTD} \propto t^{-1}$  and  $t > 0.5$  Gyr. The two free parameters can be determined by fitting the model to the rates inferred from observations. We carry out the fit using a compilation of observational determinations of the volumetric type Ia supernova rates from (Graur et al. 2014) updated with the results from the Cosmic Assembly Near-infrared Deep Extragalactic Legacy Survey (CANDLES; Rodney et al. 2014). Minimization of  $\chi^2$  with errors including statistical and systematic uncertainties yields  $\eta_0 = 1.02^{+0.27}_{-0.15} \times 10^{-4} h_7^2 \text{ yr}^{-1} M_\odot^{-1}$  and  $\eta_1/\eta_0 = 11.98^{+3.37}_{-4.49}$ . Fig. 1 compares the resulting best fit model to the observational data. The obtained constraints imply a fraction of prompt supernovae  $f_p = 0.63^{+0.07}_{-0.11}$ , consistent with the results obtained by Rodney et al. (2014).

The rate of core-collapse supernovae is directly proportional to the star formation history  $\psi(z)$ :

$$n_{\text{SNCC}}(z) = k_{\text{CC}}\psi(z), \quad (12)$$

where  $k_{\text{CC}}$  is the number of stars that explode as supernovae per unit mass. For our study, we adopt  $k_{\text{CC}} = 0.0068 M_\odot^{-1}$  expected for a mass range of supernova progenitors ( $8 M_\odot$ ,  $40 M_\odot$ ) and a Salpeter initial mass function. Since the same initial function was consistently assumed in the derivation of the star formation rate from observations, the predicted rate of core-collapse supernovae is practically independent of the initial mass function (Madau & Dickinson 2014). The resulting core-collapse supernova rate is shown in Fig. 1.

We calculate light curves and K-corrections of simulated type Ia supernovae (normal branch) using a time series of spectral templates computed by Nugent et al. (2002). Following Goldstein & Nugent (2017), we assume that the absolute magnitude is normally distributed with a mean of  $-19.3$  in the  $B$  band and a scatter of  $0.2$ . We also check the impact of using a more realistic distribution with 3 times longer Gaussian tail at low luminosities accounting for faint supernovae in volume-limited samples (see e.g. Li et al. 2011; Goldstein & Nugent 2017). For core collapse supernovae, we consider types Ib/c, IIP, IIL and IIn, assuming that their relative contributions to the total number density of core collapse supernovae are independent of redshift and constrained by low-redshift observations resulting in 16, 49, 9 and 5 per cent respectively for Ib/c, IIP, IIL and IIn (Graur et al. 2017; Li et al. 2011). We realize light curves of the four supernova subclasses using spectral templates from a compilation which is an extension of the work

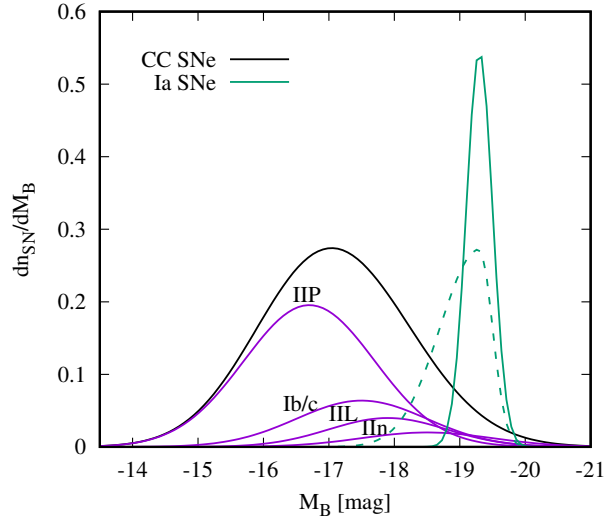


**Figure 2.** Distribution of absolute luminosities in the  $B$  band of the different types of supernovae considered in our study. Normalizations of the distributions are proportional to the local volumetric rates of the corresponding supernova classes. The green dashed curve shows an alternative model for type Ia supernovae with a tail accounting for low-luminosity supernovae.

by Nugent et al. (2002)<sup>1</sup>, based primarily on data from Levan et al. (2005) for type Ib/c, Di Carlo et al. (2002) for IIn and Gilliland et al. (1999) for the remaining two types. We approximate the distribution of absolute magnitudes in the  $B$  band by Gaussians with mean and scatter of  $-17.50$  and  $1.0$  for type Ib/c,  $-16.70$  and  $1.0$  for type IIP,  $-17.9$  and  $0.90$  for type IIL,  $-18.5$  and  $1.0$  (after discarding two outliers with  $M_B = -15.1, -22.2$ ) for IIn (Richardson et al. 2014a, for  $h = 0.73$ ). The assumed luminosity functions for all classes of supernovae are shown in Fig. 2. We note that the borderline between different classes may not be entirely clear cut. For example, there may be a continuous transition between type IIP and type IIL supernovae (e.g., Anderson et al. 2014). In this sense, these types can be seen as being representative for the fainter and more luminous ends of the type II supernova population.

### 3.3 Computation

First, we generate a random sample of lens galaxies at redshifts  $z < 1.2$ . We find that it is sufficient to realize  $10^5$  lens galaxies and then rescale the final counts of strongly lensed supernovae according to the actual number of lens galaxies contained in the assumed comoving volume. Then, we populate the observational cone up to redshift  $z = 3$  with supernovae. In order to reduce shot noise, we artificially increase the supernovae rate by a factor of  $5 \times 10^5$ . The actual detection rate is then retrieved by scaling down the counts by the same factor. In order to save computational time (driven primarily by lensing computations), we discard all supernovae at angular distances larger than  $4\theta_E$ . These supernovae are typically too far from the lenses to be

<sup>1</sup> [https://c3.lbl.gov/nugent/nugent\\_templates.html](https://c3.lbl.gov/nugent/nugent_templates.html)

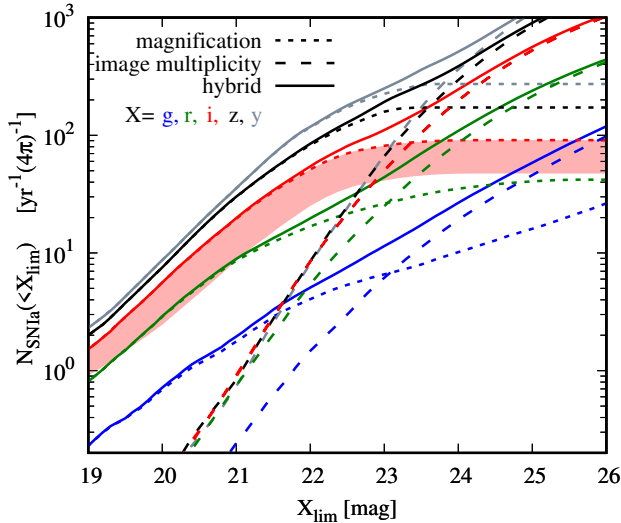


**Figure 3.** Detection rates of strongly lensed type Ia supernovae as a function of survey depth in five different bands, in an all-sky search. The long and short dashed curves compare the supernovae yields expected for two different observational strategies based on detecting image multiplicity or highly magnified supernovae. The solid curves show the yields for the hybrid method which maximizes detection rates by means of combining both detection criteria. The shaded band indicates the range of detection rates given by the extent to which flux is integrated over the supernova images, with the upper and lower limits corresponding to the total measured flux from all images (upper limit) or solely from the brightest image (lower limit).

multiply imaged or strongly magnified. Our choice of a maximum redshift for the lenses and the supernovae allows us to determine detection rates of strongly lensed supernovae for limiting magnitudes up to 26, which is around 2 mag deeper than the envisaged depth for the LSST.

For every lens-supernova pair we calculate all basic lensing properties, i.e. image multiplicity, magnifications, positions of the images and time delays. The lensing equations are solved numerically using the publicly available code for lensing calculations, *glafic* (Oguri 2010). When calculating time dependent apparent magnitudes, we take into account both the effects of magnification and time delay determined for every image.

Once the complete Monte Carlo sample of strongly lensed supernovae is computed, we can employ different detection criteria and thus determine the number of detectable lensed supernovae as a function of survey depth in several different bands. This part of the calculations is independent of the assumed cosmological model and volumetric supernova rates; therefore, it can be repeated for different detection criteria using the same precomputed Monte Carlo sample of strongly lensed supernovae and the corresponding lensing properties. The supernova yields are computed for observations in five SDSS/LSST filters: *g*, *r*, *i*, *z* and *y*.

## 4 RESULTS

### 4.1 Type Ia supernovae

Fig. 3 compares detection rates for strongly lensed type Ia supernovae expected for the three methods with the base choice of free parameters, as outlined in Section 2. Our results demonstrate that the method based on detecting highly magnified supernovae surpasses the image multiplicity technique for relatively shallow surveys with limiting magnitudes  $\lesssim 22$ . In particular, for a survey with a 21 magnitude depth, the magnification method is expected to find  $\sim 20$  times more strongly lensed supernovae than the image multiplicity method. Due to the stronger dependence on the limiting magnitude for the image multiplicity method, this ratio becomes larger for even shallower surveys, with a 3-fold change per magnitude in the *i* band.

For limiting magnitudes  $\gtrsim 23$ , increasing survey depth does not improve the performance of the magnification method, but it appreciably increases the rates for the other method. For deep surveys like the LSST, detecting multiple images appears to become a more powerful means for finding lensed type Ia supernovae than gravitational magnification. The image multiplicity method is expected to yield about twice as many detections as the magnification method at a limiting magnitude of 24. The difference between the two methods becomes even more prominent for deeper surveys: the rates expected for the image multiplicity method increase exponentially with limiting magnitudes in a range between 24 and 26, whereas the rates from the magnification method become constant.

Both methods are expected to find comparable numbers of lensed type Ia supernovae at limiting magnitudes between 23.0 in the *g* band to 23.8 in the *y* band. The lensed supernova samples returned by the two methods happen to be only weakly overlapping; therefore, combining both detection criteria is expected to increase the yields, especially at intermediate limiting magnitudes. This is demonstrated by the solid curves which show detection rates for the hybrid method which identifies strongly lensed supernovae either as highly magnified or multiply imaged transients. The hybrid method maximizes supernova yields at all limiting magnitudes. Unsurprisingly, it follows closely the rates from the magnification method at  $X_{\text{lim}} \lesssim 21$  and the image multiplicity technique at  $X_{\text{lim}} \gtrsim 24$ .

The performance of the magnification method depends on the choice of the number of images that contribute to the total flux in the observations. The red band in Fig. 3 shows the expected range of the rates modulated by this effect. The upper limit corresponds to detections based on flux integrated over all images, whereas the lower limit is expected for detections based on flux solely from the brightest image. The average ratio between the upper and lower limits is 2, with a very weak dependence on survey depth and filters.

The apparent differences between detection rates from the two main methods reflect the fact that gravitational magnification and image multiplicity are not equally prominent features of strong lensing at different depths. The relatively poor performances of the magnification method for deep surveys ( $X_{\text{lim}} > 23$ ) or the image multiplicity method for shallower surveys ( $X_{\text{lim}} < 23$ ) cannot be appreciably improved by modifying the criteria for selecting the candidates. We demonstrate these intrinsic limitations in Fig. 4,

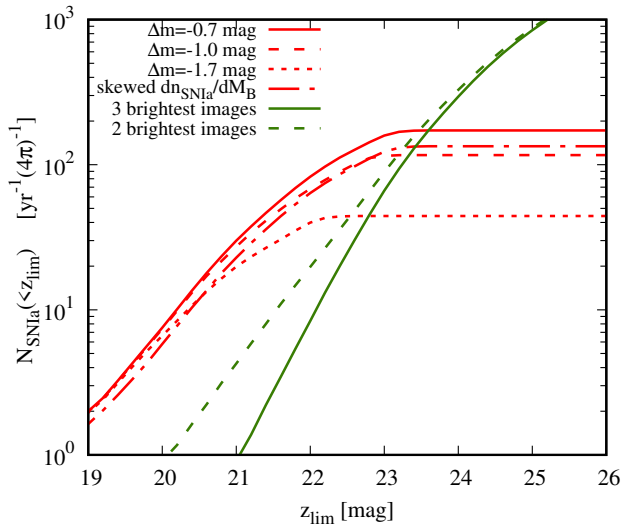


**Figure 4.** Sensitivity of detecting lensed type Ia supernova in the  $z$  band to parameters and conditions defining detection criteria of the two methods based on selecting highly magnified (red curves) or multiply imaged supernovae (green curves). The parameter  $\Delta m$  is a minimum enhancement of the apparent brightness due to lensing magnification relative to the mean magnitude of type Ia supernovae expected in the apparent host (lens) galaxy ( $\Delta m = -0.7$  for the base model). For the image multiplicity method, discovery rates depend on the minimum number of detectable images. The solid and dashed curves compare the two cases for which at least three (base model) or two images are detectable for quads and cusps. The red dashed-dotted curves shows the impact of accounting for the possible low-luminosity tail in the luminosity function  $dn_{\text{SNIa}}/dM_B$  of type Ia supernovae (see the green dashed curve in Fig. 2) on the expected discovery rates.

where we show supernova yields for different choices of the free parameters defining the detection criteria in the two methods. Reducing the magnitude gap  $\Delta m$  in the magnification method results naturally in a higher detection rate. However, the improvement is limited solely to magnitudes  $\gtrsim 22$  where the method is clearly outperformed by the image multiplicity technique. Furthermore, this inevitably leads to a higher false positive detection rates due to intrinsically bright type Ia supernovae.

Relaxing the selection criteria for the image multiplicity method by including all systems with at least two detectable images (for all images configurations) improves the supernova yields only at small limiting magnitudes, e.g. by a factor of 4 at  $z_{\text{lim}} \approx 21$  (see the green dashed curve in Fig. 4). The resulting detection rates, however, are still smaller than those of the magnification method. Since the selection criterion cannot be relaxed even further, this case sets an upper limit for the expected detection rates based on image multiplicity. Finally, we find that changing the range of the maximum image separation does not appreciably modify the predictions for the lensed supernova yields.

A strong limitation of the magnification method is reflected by a plateau at  $X_{\text{lim}} \gtrsim 22.5$  which signifies that the method does not benefit from increasing survey depth. This feature is an unavoidable drawback of the method and it cannot be removed by simply adjusting  $\Delta m$  (subject to a reasonable condition  $\Delta m < 0$ ). It is primarily caused by the fact

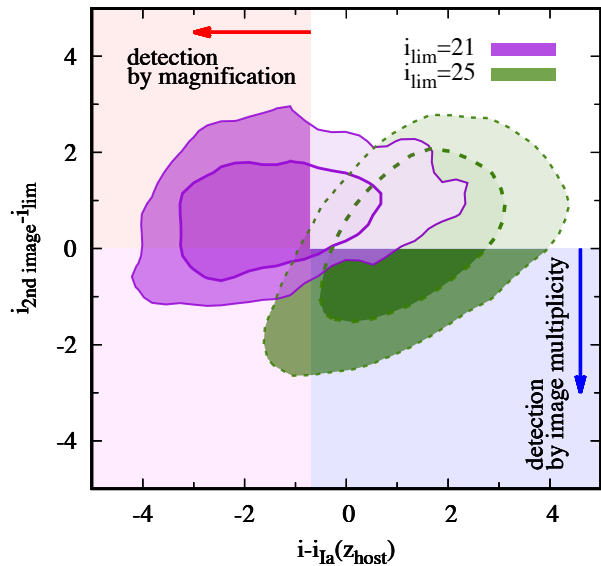


**Figure 5.** Selection of lensed supernova candidates (using type Ia as an example) by means of finding highly magnified transients, i.e. brighter than a fiducial type Ia supernovae observable in the apparent host (actual lens) galaxy (see the red arrow and the indicated shaded region), or detecting the second brightest image (see the blue arrow and the indicated shaded region). The two contours show the distribution of all observable lensed supernovae in two surveys with depths of 21 and 25 in the  $i$  band. The majority of bright, low-redshift supernovae appear to be highly magnified, but featuring the secondary image beyond detection limits (purple contours). They can be found using primarily the magnification method. On the other hand, the majority of faint, high-redshift lensed supernovae from a deep survey (green contours) are not sufficiently magnified to be detected as peculiarly bright supernovae, but they exhibit detectable second brightest images. These lensed supernovae can be effectively found as doubly imaged transients.

that high-redshift lenses and supernovae require extremely large, and therefore improbable, magnifications in order to fall within a range of detectable fluxes. We illustrate this in Fig. 5 which compares selections of lensed supernova candidates in shallow ( $i_{\text{lim}} = 21$ ) and deep ( $i_{\text{lim}} = 25$ ) surveys. Faint, high-redshift supernovae are not sufficiently magnified in order to be selected by the magnification method. Most of them happen to be fainter than a fiducial reference type Ia supernova with absolute luminosity  $M_B = -20$  that would be observed in the apparent host galaxy (actual lens galaxy). On the other hand, faint supernovae from deep surveys appear to exhibit relatively brighter secondary images than those from shallow surveys. This makes the image multiplicity method more effective in selecting lensed supernova candidates in deep surveys at  $X_{\text{lim}} \gtrsim 23.5$ .

In order to show more quantitatively the differences between the magnification and image multiplicity methods of selecting lensed supernovae candidates, we calculate the completeness of lensed supernova searches as a function of survey depth (see Fig. 6). We define the 100 percent complete reference sample as consisting of all observable/detectable lensed type Ia supernovae, i.e. all multiply imaged type Ia supernovae that are brighter than  $X_{\text{lim}}$  at the peak of their light curves in at least one of the five

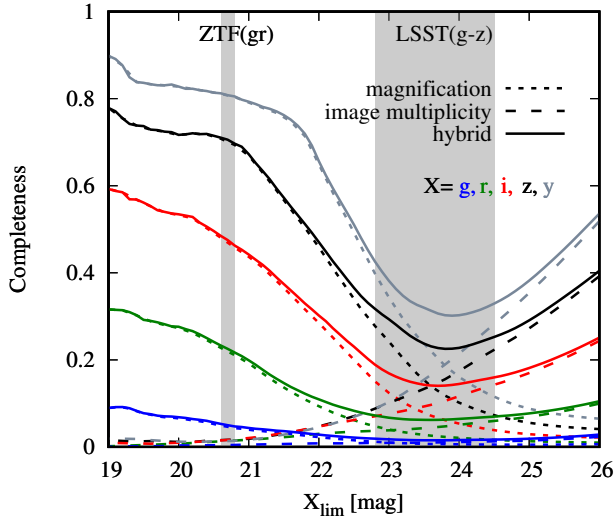


**Figure 6.** Completeness of lensed supernova candidates found with three different methods, as a function of survey depth in five different bands. The vertical grey bands indicate the depths of ZTF and LSST. The method based on detecting highly magnified supernovae reaches an  $\sim 80$  per cent completeness in the  $z$ ,  $y$  bands at  $X_{\text{lim}} < 21$ . The completeness of lensed supernovae search by means of detecting image multiplicity increases with survey depth. The method becomes more complete than that based on magnification for surveys with depths comparable to or larger than the LSST.

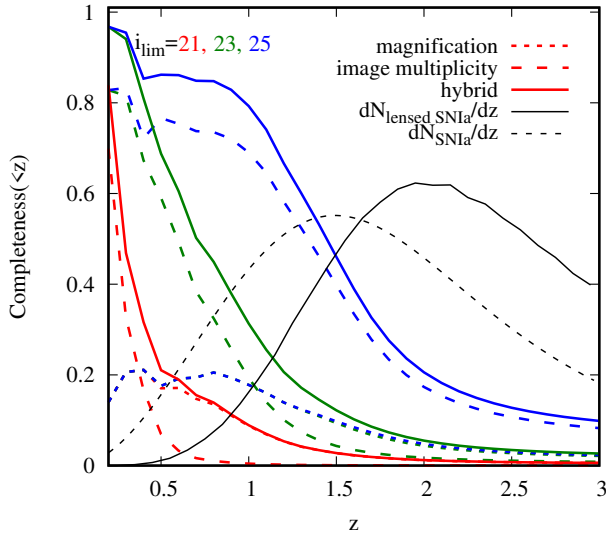


**Figure 7.** Redshift completeness of lensed type Ia supernova candidates found with three different methods, for three limiting magnitudes  $i_{\text{lim}}$  in the  $i$  band. The method based on detecting image multiplicity returns nearly complete redshift samples up to a maximum redshift set by the survey depth. For a reference point, the black curves show redshift distributions of all (non-lensed) or strongly lensed type Ia supernovae, both normalized to 1 at  $z < 3$ .

bands, where apparent magnitudes are computed by integrating flux over all images. The figure shows that the magnification method maximizes its completeness for shallow surveys, with completeness reaching 80 per cent at  $\lesssim 21.5$  mag in the  $z$  or  $y$  band, and then it degrades at large survey depths. An inverse trend characterizes the completeness of the image multiplicity method which becomes more complete with increasing survey depth, reaching about 40 per cent at 25 mag in the  $y$  or  $z$  bands. The solid curves show the completeness of the hybrid method. It is evident that combining the magnification and the image multiplicity detection criteria improves the completeness at limiting magnitudes characteristic for the LSST, i.e.  $22 < X_{\text{lim}} < 24$ . In particular, the hybrid method boosts the completeness by about 50 per cent in the  $y$  band relative to lensed supernova searches based solely on the magnification or image multiplicity criterion. Figure 7 demonstrates also a difference between the magnification and image multiplicity methods in terms of redshift completeness. While the magnification technique can never be more complete than 20 per cent at all redshifts, the image multiplicity method attains an 80-90 per cent completeness up to a maximum redshift set by the survey depth.

## 4.2 Core-collapse supernovae

In Fig. 8, we show the expected detection rates for lensed core-collapse supernovae, divided into four subclasses. As for Type Ia supernovae, the method of finding lensed supernovae by means of detecting highly magnified transients appears to be more effective for shallow surveys, but it is surpassed by the technique based on image multiplicity for deep surveys. The limiting magnitude of comparable performances of the two methods depends weakly on the supernovae type and filter, and it typically falls within a magnitude range between 23 and 24. The exception in this respect are type II $n$  supernovae for which the magnification-based method appears to be more effective up to as high as 25 magnitude in the  $g$  and  $r$  bands.

The orange curves in Fig. 8 show reference rates for lensed type Ia supernovae detectable in the  $i$  band. Except for type II $n$  supernovae, the discovery rates of lensed core-collapsed supernovae are lower than type Ia by a factor of 2-5. A high fraction of luminous type II $n$  supernovae with  $M_B < -20$  makes them appreciably easier to detect. Furthermore, the high UV flux of these supernovae substantially increases the detection rates in shorter wavelength filters. This considerably reduces the differences between detection rates in the  $g$  and  $y$  bands, which is otherwise conspicuous for all other supernova types. This effect becomes particularly strong at large limiting magnitudes ( $X_{\text{lim}} > 23.5$ ), where the  $g$  band appears to be the most effective filter for detecting lensed type II $n$  supernovae via the magnification method.

The total number of detectable lensed core-collapse supernovae exceeds that of type Ia, with the primary contribution coming solely from type II $n$  supernovae. The detection rates of lensed supernovae of type IIP, IIL and Ib/c are systematically lower than type Ia.



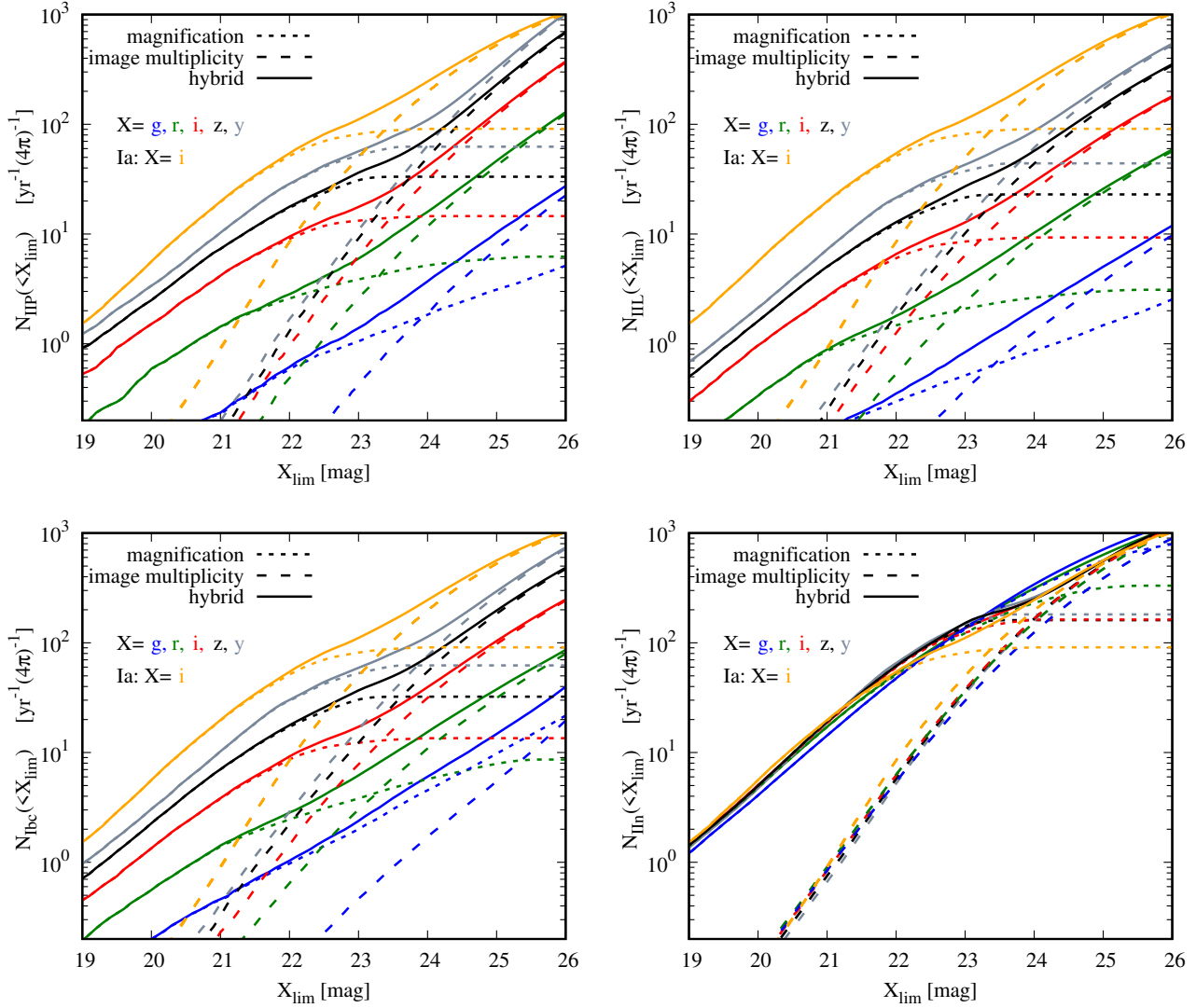


**Figure 8.** Detection rates of strongly lensed core-collapse supernovae (from top left clockwise: IIP, IIL, IIn and Ibc) as a function of survey depth in five different bands, in an all-sky search. The long and short dashed curves compare the supernova yields expected for two different observational strategies based on detecting image multiplicity or highly magnified supernovae. The solid curves show the yields for the hybrid method which maximizes detection rates by means of combining both detection criteria. For comparison, the orange curves shows the expected rates for lensed type Ia supernovae observed in the *i* band.

### 4.3 Fitting function

For the purpose of future studies exploring the feasibility of using strongly lensed supernovae as cosmological and astrophysical probes, we provide a set of simple fitting functions reproducing the computed detection rates. We find that the logarithm of detection rates can be well fitted by a fourth degree polynomial, i.e.

$$\log_{10} n_{\text{SN}}(< X_{\text{lim}}) = \sum_{i=0}^{i=4} X_i (X_{\text{lim}} - 22.5)^i. \quad (13)$$

Table A1 lists best fit parameters for different detection strategies, supernova types and filters.

The fitting functions provide accurate approximations to the exact results in a range between  $X_{\text{lim}} = 19$  and  $X_{\text{lim}} = 26$  for all cases. The mean precision given by the root mean

square averaged over all cases of filters, supernova types and methods is 0.02 dex.

## 5 DISCUSSION

The expected detection rates of strongly lensed supernovae computed in our work depend on a range of assumptions. The cosmological model, the lens model and the volumetric rates of type Ia supernovae are fairly well constrained by observations and supported by solid theoretical frameworks. On the other hand, the luminosity functions and fractions of different types of supernovae, the volumetric rates of core-collapse supernovae at high redshifts and the spectral templates of different types of core-collapse supernovae (especially type II) are less certain and may be a source of additional systematic errors in our estimates. Fig. 4 shows an

example of how modifications in the input luminosity function of type Ia supernovae can change the expected discovery rates. Bearing in mind that our results may be subject to improvements in the light of future observations, we stress that the predicted discovery rates of lensed supernovae presented here reflect the current state of our knowledge on different types of supernovae.

In our calculations we neglect the effect of microlensing. This is a safe assumption, because due to its stochastic nature, microlensing is expected to have a negligible impact on overall predictions of discovery rates of lensed supernovae (Goldstein et al. 2018b). However, the effect does perturb light curves independently in every supernova image, giving rise to additional systematic errors in measurements of relative fluxes in the images and time delays (Pierel & Rodney 2019). In our comparison of detection methods we do not consider the problem of possible false detections. All methods will be affected by a population of faint quasars increasing stochastically their brightness above the detection limit. Moreover, the magnification method can easily confuse non-lensed superluminous supernovae with high-redshift lensed candidates. Quantitative analyses of these effects is worth carrying out in the near future.

In the following, we compare observational strategies for detecting lensed supernovae in the context of ongoing or upcoming transient surveys and the potential of using lensed supernovae for cosmological inference.

### 5.1 Ongoing and upcoming surveys

Strongly lensed supernovae will be discovered in appreciable numbers by ongoing and upcoming transient surveys. Table 1 lists the expected discovery rates for the Zwicky Transient Facility (ZTF), LSST and a hypothetical Pan-STARRS survey.

ZTF is an ongoing survey monitoring 15000 deg<sup>2</sup> in the *g* and *r* bands. For the estimation of discovery rates, we assume that all candidates will be detected in the most effective filter, i.e. the *r* band. A  $5\sigma$  limiting magnitude per pointing in this survey is 20.6 (Bellm et al. 2019). As a Pan-STARRS-based survey example, we consider a strategy which is alternative to ZTF. The sky coverage is only 20 per cent of that in ZTF, but in *griz* bands with the same cadence as ZTF. All lensed supernovae detectable in this survey would be found in the *i* band for which the survey would reach a  $5\sigma$  limiting magnitude of 20.6 per pointing. The potentially more effective *z* band would not improve detection rates due to its shallower depth of 20.2. Both ZTF and the Pan-STARRS survey operate in the regime of limiting magnitudes at which the only effective detection technique is the magnification method. Therefore, we omit the rates expected for the image multiplicity and hybrid techniques for them in Table 1.

LSST will cover about 20000 deg<sup>2</sup> in 6 *ugrizy* bands every 2–3 weeks with a limiting magnitude of 24 (LSST Science Collaboration et al. 2009, 2017). Precise estimation of discovery rates relies on details of the observational strategy which is yet to be decided. However, reasonable estimates can be obtained based on the following reasoning. A typical redshift of strongly lensed supernovae to be discovered by LSST is  $z = 1$ . This means that the faintest supernovae can be detected only within a time window of about 10 days

(rest frame) around the peak of their light curve (20 days in the observer frame). In order to satisfy this condition, all detectable supernovae should be at least 0.2 mag brighter at the peak than the actual limiting magnitudes of the survey which are (24.5, 24.2, 23.6, 22.8, 22.0) in the *grizy* bands (mean  $5\sigma$  per pointing; based on LSST collaboration’s simulations, baseline2018a run<sup>2</sup>, which is the current official reference simulated survey). Then, the expected discovery rate can be found as the maximum rate found for all filters. Since LSST will observe down to limiting magnitudes at which the image multiplicity method becomes effective, we provide rate estimates for all three methods of finding lensed supernova candidates. Table 1 also shows the most effective filter (with the highest rate) for different supernova types and detection methods.

Pre-LSST surveys may find about 5 strongly lensed supernovae per year, based solely on the magnification method. The most frequent type will be II<sub>n</sub>, followed by Ia. Discovery rates will increase by nearly two orders of magnitude for LSST. It is also clear that the magnification method is expected to yield only about 2 times more discoveries than the image multiplication method. However, both methods will detect lensed supernovae at comparable rates when we assume that the measured flux in the magnification methods comes solely from the brightest image (see Fig. 3). Furthermore, keeping in mind that multiply imaged transients do not require follow-up observations confirming their lensing nature (in contrast to highly magnified transients which can be confused with superluminous supernovae) we conclude that *the image multiplicity method will be the most effective technique for finding lensed transients in LSST data.*

Lensed supernovae discovered by LSST will be typically detected in the *i* band as a multiply imaged transient and in the *y* band (or the *z* band for type Ia and IIP) as a highly magnified transient (except for type II<sub>n</sub> which will be discovered primarily in bluer filters). The difference in the effective discovery band can strengthen the complementarity of the two detection techniques. Considering a hybrid method of finding lensed supernovae via image multiplicity in the *i* band and magnification in the *y* band (or *z* for Type Ia and IIP), we find that discovery rates in this approach are higher by 30–50 per cent than those based solely on magnification.

Except for type IIP supernovae, our discovery rates estimated for ZTF and LSST based on the magnification method agree fairly well with analogous predictions obtained by Goldstein et al. (2018a). Adopting the same detection conditions and survey parameters for LSST, we also recover fairly closely the rates estimated by Oguri & Marshall (2010), with the total number of lensed Type Ia and core-collapse supernovae to be discovered by LSST of 32 and 36. These rates are lower by a factor of  $> 10$  than those listed in Table 3 and obtained by Goldstein et al. (2018a). These differences can be fully accounted for to the stricter detection criteria adopted by Oguri & Marshall (2010), i.e. an effective limiting magnitude of 22.6 in the *i* band (in order to sample light curves at minimum depth of 0.7 mag around the peak) and an effective survey time of 2.5 years (accounting for seasonal changes of the surveyed area), and

<sup>2</sup> <https://www.lsst.org/scientists/simulations/opsim/opsim-survey-data>

survey/detection method	effective area	Type Ia	Type IIP	Type IIL	Type Ib/c	Type IIn
ZTF/magnification	15 000 deg <sup>2</sup>	2.1 ( <i>r</i> )	0.37 ( <i>r</i> )	0.23 ( <i>r</i> )	0.36 ( <i>r</i> )	3.8 ( <i>r</i> )
Pan-STARRS/magnification	3000 deg <sup>2</sup>	0.9 ( <i>i</i> )	0.20 ( <i>i</i> )	0.13 ( <i>i</i> )	0.20 ( <i>i</i> )	0.8 ( <i>i</i> )
LSST/magnification	20 000 deg <sup>2</sup>	61 ( <i>z</i> )	12.2 ( <i>z</i> )	8.7 ( <i>y</i> )	12.3 ( <i>y</i> )	184 ( <i>g</i> )
LSST/image multiplicity	20 000 deg <sup>2</sup>	44 ( <i>i</i> )	6.1 ( <i>i</i> )	5.5 ( <i>i</i> )	6.8 ( <i>i</i> )	88 ( <i>g</i> )
LSST/hybrid	20 000 deg <sup>2</sup>	89 ( <i>iz</i> )	16.3 ( <i>iz</i> )	11.9 ( <i>iy</i> )	15.8 ( <i>iy</i> )	210 ( <i>g</i> )

**Table 1.** The expected *annual* numbers of discovered lensed supernovae in ongoing or upcoming transient surveys. The method based on image multiplicity is ineffective in case case of ZTF and Pan-STARRS, and thus it is omitted in the table. Symbols in parentheses indicate the most effective filter yielding the largest number of detections.

do not signal discrepancies in the basic methodologies in the independent approaches to estimating detection rates. It is worth mentioning that more restrictive selection criteria than those proposed by Oguri & Marshall (2010) are required for obtaining high quality measurements of gravitational time delays. In particular, a minimum precision of 5 per cent and an accuracy of 1 per cent in the time delay measurements (if based solely on LSST observations) would reduce the number of lensed type Ia supernovae to about 1 per year (Huber et al. 2019). This rate can be increased by a factor of 2–16 by employing other instruments for follow-up observations.

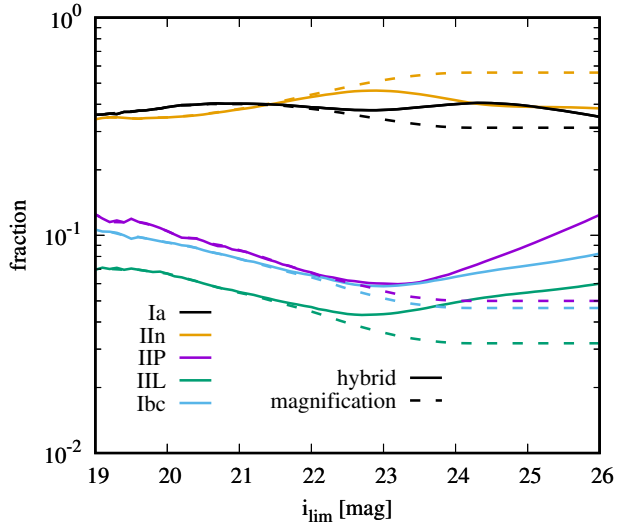
## 5.2 Observed fractions of supernova types

Fig. 9 shows predicted fractions of different types of supernovae in representative samples of gravitationally lensed supernovae expected in transient surveys with a range of limiting magnitudes between 19 and 26.

The observed fractions depend quite weakly on limiting magnitude. The most noticeable trend occurs for type IIP, IIL and Ibc at large limiting magnitudes for the image multiplicity method. The highest fractions of these supernovae are expected for extremely shallow or deep surveys.

Type Ia and IIn supernovae clearly dominate detections, with fractions of about 30 per cent each. The prevalence of type IIn supernovae becomes even stronger Ia when one includes detections in the *g* band, the most efficient filter for observing type IIn supernovae. We emphasize that the high relative discovery rates of type IIn supernovae rely quite strongly on the adopted spectral templates which in turn depend on the extinction correction performed in the analysis of the observational data used here (see Di Carlo et al. 2002).

Nevertheless, the high predicted relative detection rates of lensed type IIn supernovae is intriguing. The rates and luminosity distribution of type IIn supernovae at high redshift are quite uncertain, theoretically because of their wide range of possible progenitors, including very massive stars in the tail of the initial mass function (e.g., Gal-Yam & Leonard 2009; Smith 2014; Thöne et al. 2017) and observationally, because of their diverse photometric properties (e.g., Taddia et al. 2013; Richardson et al. 2014b; Cappellaro et al. 2015). Fortunately, lensed type IIn supernovae can readily be distinguished from other supernovae due to their narrow (and hence high spectroscopic signal-to-noise ratio) Balmer emission lines. Hence, observations of lensed IIn could provide unique insights into their intrinsic properties at high redshift.



**Figure 9.** Fractions of different supernova types in samples of gravitationally lensed supernovae detected in transient surveys with limiting magnitude  $i_{\text{lim}}$  in the *i* band. Gravitationally lensed supernovae are detected via magnification (dashed curves) or using the hybrid method (solid curves).

## 5.3 Discovery space

The detection methods considered in this study may also lead to differences in the phase space of lensing configurations. Fig. 10 shows the distributions of basic lensing parameters of lensed type Ia supernovae as a function of limiting *i*-band magnitude. The green contours show 10-quantiles of the distributions expected for the hybrid method. The purple and orange curves show the median and a range containing 80 per cent of the cases for the magnification and image multiplicity techniques, respectively. We omit results for the image multiplication technique at limiting magnitudes lower than  $i_{\text{lim}} = 21.5$  where the method is far less competitive, with the potential discovery rate smaller than 10 per cent of that of the magnification technique. Fig. 10 also shows the fractions of the different image configurations with two (doubles), three (cusps) and four images (quads).

Gravitationally lensed supernovae to be found in ongoing pre-LSST shallow surveys will be extremely magnified. For a limiting magnitude of 20.6 (depth of ZTF), the expected mean magnification is 20 and a 10 per cent tail of the distribution includes cases with magnifications exceeding 100. For shallower surveys, the expected magnification become substantially higher with the mean reaching  $\mu = 100$  at  $i_{\text{lim}} = 19.5$ .

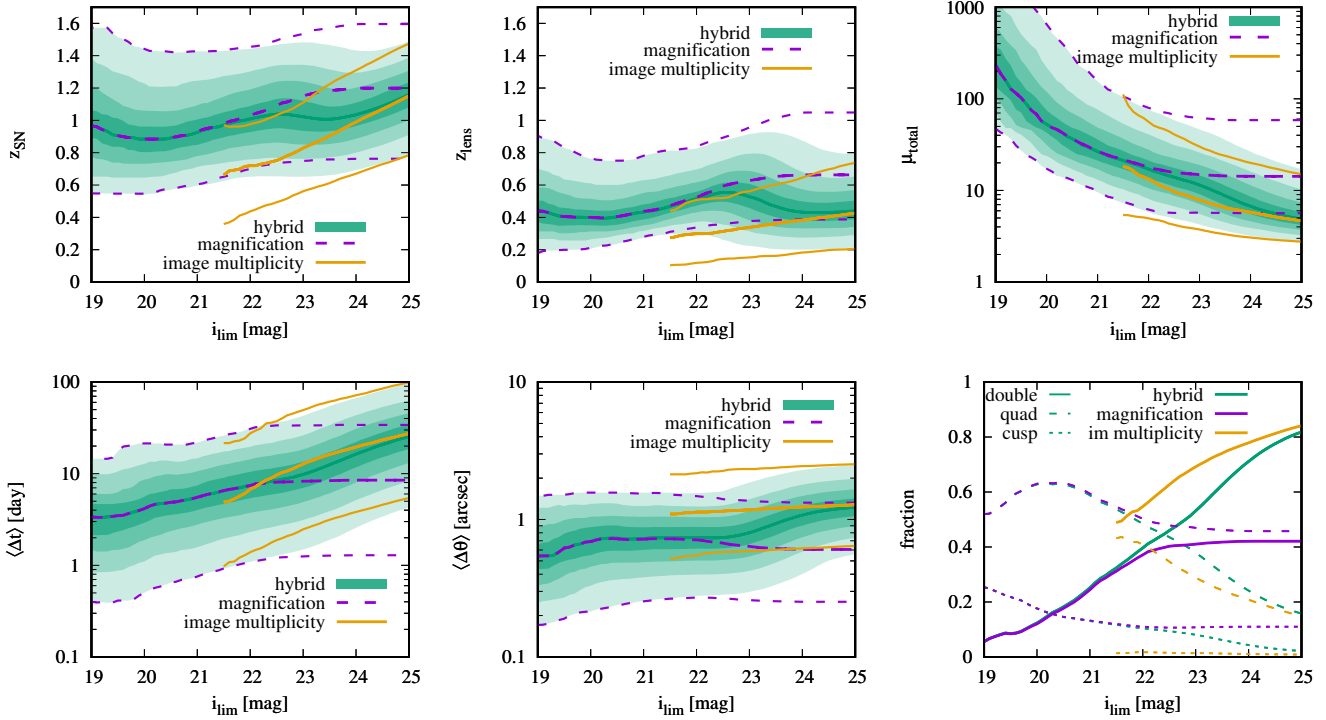


**Figure 10.** Discovery space of gravitationally lensed type Ia supernovae detected with different methods in a single-filter survey with depth  $i_{\text{lim}}$  in the  $i$  band. The panels show distributions of supernova redshift  $z_{\text{SN}}$ , lens redshift  $z_{\text{lens}}$ , total magnification  $\mu_{\text{total}}$ , gravitational time delay averaged over all image pairs  $\langle \Delta t \rangle$  and image separation averaged over all image pairs  $\langle \Delta \theta \rangle$ . The green contours show 10-quantiles of the distributions for supernova samples produced by the hybrid method. The purple and orange curves show the median and 80-percent probability range of probability distributions for the magnification and image multiplicity methods, respectively. The results for the image multiplicity are shown only for detection rates larger than 10 per cent of the corresponding detection rates for the magnification method. The bottom right panel shows fractions of different lensing configurations with two images (doubles), three images (cusps) or four images (quads).

The expected lensing properties of lensed supernovae detected via magnification pose a challenge to using them as cosmological probes. In particular, the typical time delays for lensed supernovae found in pre-LSST surveys are below 10 days and typical image separations will hardly exceed the arcsec scale. Fig. 10 demonstrates that LSST or deeper surveys – with typical time delays always below 10 days – can hardly mitigate this problem. In this respect, the image multiplicity method appears to be more promising. When applied to LSST-like surveys ( $i_{\text{lim}} = 23.5$ ), the method is expected to find lensed supernovae with the mean time delay of 20 days (and a 10 per cent tail of the distribution with time delays at least 60 days) and typical image separations larger than 1 arcsec. Undoubtedly, this increases the potential for using lensed supernovae to place robust cosmological constraints.

Time delays and image separations are not the only differences between the populations of lensed supernovae found via magnification and image multiplicity. We also find that the image multiplicity method is more sensitive to supernovae and lens galaxies at lower redshifts. There is also a clear difference in terms of image configuration. A much larger fraction of lensed supernovae found via image multiplicity are doubles, whereas for the magnification methods the numbers of quads and doubles are comparable. Unsurprisingly, both methods exhibit an increasing (decreas-

ing) trend in the fraction of doubles (quads) with increasing limiting magnitude. The fraction of cusps is at the sub-percent level for the image magnification methods, whereas it reaches a 10-percent level for the magnification technique.

In the context of discussing the future phase space of lensing configurations, it is interesting to consider the case of the gravitationally lensed supernova iPTF16geu. The supernova was discovered in a relatively shallow survey. In this respect, its high magnification of  $\mu_{\text{total}} \sim 50$  is not surprising. However, the observed magnification turns out to be at odds with the theoretical expectations when the redshift of the supernova is taken into account (More et al. 2017; Goldstein et al. 2018a). In order to address this tension, we compute two-dimensional credibility contours for redshifts and gravitational magnifications of all lensed supernovae detectable in a transient survey equivalent to the intermediate Palomar Transient Factory. As a nominal depth of the survey, we consider either 20.5 or 20.0 in the  $r$  band. The latter is a more appropriate choice when one requires good observations of light curves around the peak (More et al. 2017). The supernova was discovered as a peculiarly bright, initially unresolved, transient; therefore, it is justified to employ the magnification method as an effective approach to finding lensed transients in the iPTF survey. As shown in Fig. 11, the tension between iPTF16geu and theoretical predictions is at a quite modest level of  $2\sigma$ . We conclude that the pe-

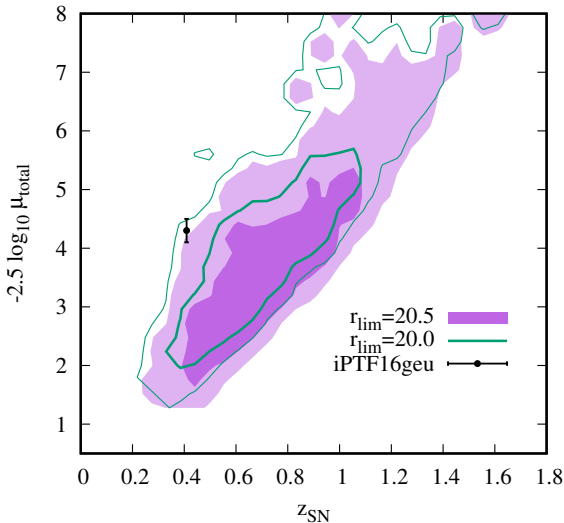


**Figure 11.** The expected distribution of the total magnification and redshift (in the form of  $1\sigma$  and  $2\sigma$  credibility contours) of lensed supernovae detectable in the intermediate Palomar Transient Factory (iPTF) survey with limiting magnitude  $r_{\text{lim}}$  in the  $r$  band, compared to the measured parameters of observed gravitationally lensed supernovae iPTF16geu. The observed supernovae lies well within a  $2\sigma$  contour.

cular lensing configuration of iPTF16geu can be simply a statistical fluke. However, the flux ratio anomalies between observed brightness of the images and the best fit lens model pose a serious problem because the discrepancy seems too large to be ascribed to microlensing (Yahalomi et al. 2017).

## 6 SUMMARY AND CONCLUSIONS

We have compared different observational strategies for detecting gravitationally lensed supernovae in massive transient surveys. The strategies rely on finding multiply imaged transients or highly magnified supernovae (deduced via comparing observed magnitudes to fiducial magnitudes of a type Ia supernova located in the apparent host galaxy). Adopting state-of-the-art models of lens galaxies constrained by the SDSS data and the standard cosmological  $\Lambda$ CDM mode, we have calculated detection rates for each method in 5 *grizy* bands for the main supernova classes including: type Ia, core-collapse supernovae types IIP, IIL, Ibc and IIn. We provide simple fitting functions approximating the computed rates.

We find that detecting lensed supernovae as strongly magnified transients is the only effective detection method working for shallow pre-LSST surveys with limiting magnitudes smaller than 22. However, the expected yields saturate at limiting magnitudes of about 23.0–23.5 (depending on supernova type and filter) where lensed supernovae are more likely to be fainter than a fiducial type Ia supernova in the apparent host galaxies (lens galaxy). At this limiting magnitude, the magnification and image multiplicity method yield comparable numbers of lensed supernovae. Supernovae found by the two methods are to a large extent independent; therefore, a noticeable improvement of discovery rates can be achieved by combining the two methods. The resulting

hybrid method increases the yields by 50 per cent at limiting magnitudes corresponding to comparable rates expected for the two primary methods. For larger limiting magnitudes  $\gtrsim 23.5$ , the image multiplicity method completely surpasses the performance of the magnification technique.

Detection rates depend strongly on filter. Except for type IIn, discovery rates decrease with decreasing effective wavelength. An inverse trend found for type IIn supernovae results from the presence of strong UV flux and a relatively higher incidence of luminous supernovae with  $M_B < -20$ . In the overall counts of gravitationally lensed supernovae, type IIn will be the most common class followed by type Ia, regardless of the adopted detection method. The rates are dominated by intrinsically bright supernovae; therefore, the robustness of our predictions rely on accurate modelling of high-luminosity tails of the supernova luminosity functions, currently approximated by Gaussian distributions.

Revisiting the initial comparison between the image multiplicity and magnification methods made by Goldstein & Nugent (2017), we find that detecting lensed supernovae via image multiplicity is as efficient as the magnification method at the limiting magnitudes of LSST and it surpasses the latter for deeper surveys. Moreover, strongly lensed supernovae found via image multiplicity are also characterized by longer time delays and larger image separations than systems found via magnification. This makes the image multiplicity method a more appealing observational strategy for LSST when considering the potential of using lensed supernovae as cosmological probes. It is also worth mentioning that the image multiplicity approach does not rely on follow-up observations and it can be naturally applied to self-contained massive surveys without auxiliary imaging observations. In contrast, candidates for lensed supernovae selected via magnification naturally require follow-up observations to confirm their the lensing nature.

We estimate that ZTF with a depth of 20.6 in the  $r$  band will detect 1.9 type Ia 4.1 core-collapse (primarily IIn) lensed supernovae per year. Analogous computations for LSST yield 44 type Ia and 106 core-collapse (primarily IIn) lensed supernovae per year, detected via image multiplicity. The hybrid method will allow to increase these rates to 89 and 254 detections per year for type Ia and core-collapse, respectively. Core-collapse lensed supernovae will be dominated by type IIn with relative fraction of 80 per cent.

## ACKNOWLEDGMENTS

We are highly indebted to the referee, Prasenjit Saha, for his insightful comments and helpful suggestions. This work was supported by a VILLUM FONDEN Investigator grant to JH (project number 16599).

## REFERENCES

- Andersen P., Hjorth J., 2018, MNRAS, 480, 68
- Anderson J. P. et al., 2014, ApJ, 786, 67
- Barbary K. et al., 2012, ApJ, 745, 31
- Belczynski K., Bulik T., Ruiter A. J., 2005, ApJ, 629, 915
- Bellm E. C. et al., 2019, Publications of the Astronomical Society of the Pacific, 131, 018002

- Bezanson R. et al., 2011, *ApJ*, 737, L31  
Blanc G. et al., 2004, *A&A*, 423, 881  
Botticella M. T. et al., 2008, *A&A*, 479, 49  
Cano Z., Selsing J., Hjorth J., de Ugarte Postigo A., Christensen L., Gall C., Kann D. A., 2018, *MNRAS*, 473, 4257  
Cappellaro E. et al., 2015, *A&A*, 584, A62  
Cappellaro E., Evans R., Turatto M., 1999, *A&A*, 351, 459  
Castro T., Martin M., Giocoli C., Borgani S., Dolag K., 2018, *MNRAS*, 478, 1305  
Chae K.-H., 2003, *MNRAS*, 346, 746  
Chen W. et al., 2019, arXiv e-prints, arXiv:1902.05510  
Choi Y.-Y., Park C., Vogeley M. S., 2007, *ApJ*, 658, 884  
Dahlen T., Strolger L.-G., Riess A. G., 2008, *ApJ*, 681, 462  
Di Carlo E. et al., 2002, *ApJ*, 573, 144  
Diego J. M., 2018, arXiv e-prints, arXiv:1806.04668  
Dilday B. et al., 2008, *ApJ*, 682, 262  
Dilday B. et al., 2010, *ApJ*, 713, 1026  
Gal-Yam A., Leonard D. C., 2009, *Nature*, 458, 865  
Gilliland R. L., Nugent P. E., Phillips M. M., 1999, *ApJ*, 521, 30  
Goldstein D. A., Nugent P. E., 2017, *ApJ*, 834, L5  
Goldstein D. A., Nugent P. E., Goobar A., 2018a, ArXiv e-prints, arXiv:1809.10147  
Goldstein D. A., Nugent P. E., Kasen D. N., Collett T. E., 2018b, *ApJ*, 855, 22  
Goobar A. et al., 2017, *Science*, 356, 291  
Graur O., Bianco F. B., Modjaz M., Shivvers I., Filippenko A. V., Li W., Smith N., 2017, *ApJ*, 837, 121  
Graur O., Maoz D., 2013, *MNRAS*, 430, 1746  
Graur O. et al., 2011, *MNRAS*, 417, 916  
Graur O. et al., 2014, *ApJ*, 783, 28  
Grillo C. et al., 2018, *ApJ*, 860, 94  
Hardin D. et al., 2000, *A&A*, 362, 419  
Holder G. P., Schechter P. L., 2003, *ApJ*, 589, 688  
Horesh A., Poznanski D., Ofek E. O., Maoz D., 2008, *MNRAS*, 389, 1871  
Huber S. et al., 2019, arXiv e-prints, arXiv:1903.00510  
Kurov A. A., Dai L., Venumadhav T., Miralda-Escudé J., Frye B., 2019, arXiv e-prints  
Keeton C. R., Kochanek C. S., Seljak U., 1997, *ApJ*, 482, 604  
Kelly P. L. et al., 2016, *ApJ*, 831, 205  
Kelly P. L. et al., 2018, *Nature Astronomy*, 2, 334  
Kelly P. L. et al., 2015, *Science*, 347, 1123  
Kochanek C. S., 1991, *ApJ*, 373, 354  
Kolatt T. S., Bartelmann M., 1998, *MNRAS*, 296, 763  
Kormann R., Schneider P., Bartelmann M., 1994, *A&A*, 284, 285  
Levan A. et al., 2005, *ApJ*, 624, 880  
Li W. et al., 2011, *MNRAS*, 412, 1441  
LSST Science Collaboration et al., 2009, arXiv e-prints, arXiv:0912.0201  
LSST Science Collaboration et al., 2017, arXiv e-prints  
Madau P., Dickinson M., 2014, *ARA&A*, 52, 415  
Maoz D., Mannucci F., 2012, *PASA*, 29, 447  
Melinder J. et al., 2012, *A&A*, 545, A96  
Mitchell J. L., Keeton C. R., Frieman J. A., Sheth R. K., 2005, *ApJ*, 622, 81  
Montero-Dorta A. D., Bolton A. S., Shu Y., 2017, *MNRAS*, 468, 47  
More A., Suyu S. H., Oguri M., More S., Lee C.-H., 2017, *ApJ*, 835, L25  
Nugent P., Kim A., Perlmutter S., 2002, *PASP*, 114, 803  
Oguri M., 2010, *PASJ*, 62, 1017  
Oguri M. et al., 2008, *AJ*, 135, 512  
Oguri M., Kawano Y., 2003, *MNRAS*, 338, L25  
Oguri M., Marshall P. J., 2010, *MNRAS*, 405, 2579  
Pain R. et al., 2002, *ApJ*, 577, 120  
Perrett K. et al., 2012, *AJ*, 144, 59  
Pierel J. R., Rodney S. A., 2019, arXiv e-prints, arXiv:1902.01260  
Quimby R. M. et al., 2014, *Science*, 344, 396  
Refsdal S., 1964, *MNRAS*, 128, 307  
Richardson D., Jenkins, III R. L., Wright J., Maddox L., 2014a, *AJ*, 147, 118  
Richardson D., Jenkins, III R. L., Wright J., Maddox L., 2014b, *AJ*, 147, 118  
Rodney S. A. et al., 2018, *Nature Astronomy*, 2, 324  
Rodney S. A. et al., 2015, *ApJ*, 811, 70  
Rodney S. A. et al., 2014, *AJ*, 148, 13  
Rodney S. A. et al., 2016, *ApJ*, 820, 50  
Rodney S. A., Tonry J. L., 2010, *ApJ*, 723, 47  
Schneider P., Sluse D., 2014, *A&A*, 564, A103  
Smith N., 2014, *ARA&A*, 52, 487  
Taddia F. et al., 2013, *A&A*, 555, A10  
Thöne C. C. et al., 2017, *A&A*, 599, A129  
Tonry J. L. et al., 2003, *ApJ*, 594, 1  
Vega-Ferrero J., Diego J. M., Miranda V., Bernstein G. M., 2018, *ApJ*, 853, L31  
Witt H. J., Mao S., 1997, *MNRAS*, 291, 211  
Yahalom D. A., Schechter P. L., Wambsganss J., 2017, arXiv e-prints, arXiv:1711.07919

## APPENDIX A: PARAMETERS OF FITTING FUNCTION

Method	SN Type	Bandpass	$X_0$	$X_1$	$X_2$	$X_3$	$X_4$
magnification	Ia	$g$	0.72036	0.24009	-0.03900	0.00477	0.00104
magnification	Ia	$r$	1.33862	0.19880	-0.04735	0.00450	-0.00012
magnification	Ia	$i$	1.83059	0.21667	-0.09311	0.00355	0.00255
magnification	Ia	$z$	2.07615	0.25577	-0.10111	0.00216	0.00285
magnification	Ia	$y$	2.23439	0.29536	-0.10980	0.00041	0.00343
multiple images	Ia	$g$	0.48173	0.61185	-0.06134	0.00563	-0.00097
multiple images	Ia	$r$	1.07923	0.67684	-0.07377	0.00196	-0.00009
multiple images	Ia	$i$	1.33432	0.80388	-0.09728	-0.01051	0.00351
multiple images	Ia	$z$	1.38904	0.88393	-0.08518	-0.01878	0.00392
multiple images	Ia	$y$	1.38537	0.94450	-0.07931	-0.02503	0.00464
hybrid	Ia	$g$	0.88408	0.37177	-0.00971	0.00149	-0.00033
hybrid	Ia	$r$	1.47731	0.36007	0.00447	0.00321	-0.00195
hybrid	Ia	$i$	1.89609	0.35927	-0.02158	0.00505	-0.00031
hybrid	Ia	$z$	2.10720	0.37109	-0.03153	0.00530	0.00018
hybrid	Ia	$y$	2.24285	0.38345	-0.04630	0.00507	0.00118
magnification	IIP	$g$	-0.09803	0.30353	-0.03839	-0.00170	0.00210
magnification	IIP	$r$	0.51297	0.18132	-0.03835	0.00365	-0.00023
magnification	IIP	$i$	1.05567	0.17664	-0.07500	0.00283	0.00206
magnification	IIP	$z$	1.37635	0.22296	-0.08338	0.00011	0.00265
magnification	IIP	$y$	1.60361	0.26657	-0.09178	-0.00201	0.00324
multiple image	IIP	$g$	-0.73742	0.74209	-0.02966	-0.00791	0.00130
multiple image	IIP	$r$	0.05035	0.79421	-0.05724	-0.01589	0.00452
multiple image	IIP	$i$	0.39685	0.85468	-0.06020	-0.01743	0.00460
multiple image	IIP	$z$	0.53709	0.87378	-0.04444	-0.01662	0.00342
multiple image	IIP	$y$	0.62664	0.86039	-0.03253	-0.01300	0.00225
hybrid	IIP	$g$	-0.03277	0.39937	0.00269	-0.00081	0.00066
hybrid	IIP	$r$	0.61623	0.33920	0.02793	0.00642	-0.00203
hybrid	IIP	$i$	1.10586	0.32201	0.00987	0.00839	-0.00064
hybrid	IIP	$z$	1.39204	0.32922	-0.00632	0.00811	0.00059
hybrid	IIP	$y$	1.60046	0.33684	-0.02764	0.00781	0.00209
magnification	IIL	$g$	-0.40183	0.23634	-0.01517	0.00582	-0.00057
magnification	IIL	$r$	0.25718	0.15857	-0.03946	0.00435	-0.00008
magnification	IIL	$i$	0.86956	0.17352	-0.07717	0.00352	0.00206
magnification	IIL	$z$	1.22347	0.22128	-0.08761	0.00140	0.00264
magnification	IIL	$y$	1.46877	0.26402	-0.09947	-0.00036	0.00340
multiple image	IIL	$g$	-0.74372	0.65666	-0.05661	-0.00358	0.00195
multiple image	IIL	$r$	0.07288	0.66921	-0.06623	-0.00301	0.00203
multiple image	IIL	$i$	0.47375	0.72861	-0.07291	-0.00444	0.00220
multiple image	IIL	$z$	0.65237	0.77378	-0.06863	-0.00711	0.00228
multiple image	IIL	$y$	0.78459	0.79863	-0.05759	-0.00825	0.00117
hybrid	IIL	$g$	-0.26604	0.36248	0.01242	0.00311	-0.00151
hybrid	IIL	$r$	0.41663	0.35667	0.01112	0.00232	-0.00097
hybrid	IIL	$i$	0.95985	0.34048	0.00086	0.00553	-0.00076
hybrid	IIL	$z$	1.26577	0.34858	-0.01301	0.00577	0.00010
hybrid	IIL	$y$	1.48178	0.35631	-0.03247	0.00597	0.00141

**Table A1.** Best fit parameters of a polynomial function approximating the computed rates of detecting strongly lensed supernovae, for different detection methods and bandpass filters. The fitting function is given by eq. (13) and the rates are in units of  $\text{yr}^{-1} (4\pi)^{-1}$  (yields from a full-sky survey per year).

Method	SN Type	Bandpass	$X_0$	$X_1$	$X_2$	$X_3$	$X_4$
magnification	Ibc	<i>g</i>	0.14709	0.31974	0.00689	0.00305	-0.00104
magnification	Ibc	<i>r</i>	0.49563	0.20613	-0.02187	0.00285	-0.00080
magnification	Ibc	<i>i</i>	1.02766	0.17760	-0.07830	0.00321	0.00219
magnification	Ibc	<i>z</i>	1.37074	0.22244	-0.08762	0.00128	0.00264
magnification	Ibc	<i>y</i>	1.61716	0.26280	-0.09812	-0.00027	0.00329
multiple images	Ibc	<i>g</i>	-0.67826	0.63296	-0.01858	-0.00064	-0.00025
multiple images	Ibc	<i>r</i>	0.16955	0.68416	-0.07132	-0.00334	0.00255
multiple images	Ibc	<i>i</i>	0.55571	0.74754	-0.07414	-0.00661	0.00290
multiple images	Ibc	<i>z</i>	0.73853	0.75590	-0.05557	-0.00484	0.00125
multiple images	Ibc	<i>y</i>	0.85114	0.77360	-0.05053	-0.00659	0.00142
hybrid	Ibc	<i>g</i>	0.19634	0.35951	0.01349	0.00263	-0.00104
hybrid	Ibc	<i>r</i>	0.62451	0.34332	0.01745	0.00303	-0.00160
hybrid	Ibc	<i>i</i>	1.09885	0.32867	-0.00133	0.00634	-0.00050
hybrid	Ibc	<i>z</i>	1.40103	0.33547	-0.01531	0.00681	0.00035
hybrid	Ibc	<i>y</i>	1.62488	0.34237	-0.03615	0.00692	0.00172
magnification	IIn	<i>g</i>	1.90814	0.45380	-0.03934	-0.00427	0.00045
magnification	IIn	<i>r</i>	1.91461	0.38611	-0.05516	-0.00382	0.00061
magnification	IIn	<i>i</i>	1.95587	0.31645	-0.10087	-0.00210	0.00325
magnification	IIn	<i>z</i>	1.98209	0.31814	-0.10942	-0.00231	0.00377
magnification	IIn	<i>y</i>	2.01341	0.33552	-0.10991	-0.00248	0.00357
multiple images	IIn	<i>g</i>	1.11411	0.72917	-0.04473	-0.00435	0.00007
multiple images	IIn	<i>r</i>	1.18910	0.75405	-0.05117	-0.00637	0.00056
multiple images	IIn	<i>i</i>	1.19611	0.78006	-0.05496	-0.00828	0.00096
multiple images	IIn	<i>z</i>	1.17156	0.79957	-0.05529	-0.00965	0.00115
multiple images	IIn	<i>y</i>	1.13596	0.81564	-0.05541	-0.01082	0.00136
hybrid	IIn	<i>g</i>	1.91431	0.46530	-0.03247	-0.00292	0.00050
hybrid	IIn	<i>r</i>	1.94418	0.42431	-0.03745	-0.00056	0.00074
hybrid	IIn	<i>i</i>	1.96332	0.37749	-0.05314	0.00379	0.00213
hybrid	IIn	<i>z</i>	1.98247	0.37635	-0.05987	0.00410	0.00260
hybrid	IIn	<i>y</i>	2.00122	0.38171	-0.06689	0.00395	0.00299

**Table A2.** Continuation of Table A1.